Constructing [2.2]Paracyclophane-Based Ultrasensitive Optical Fluorescent-Phosphorescent Thermometer with Cucurbit[8]uril Supramolecular Assembly

Xujun Qiu, Teng Zheng,* Marcin Runowski,* Przemysław Woźny, Inocencio R. Martín, Kevin Soler-Carracedo, Claudia Espinosa Piñero, Sergei Lebedkin, Olaf Fuhr, and Stefan Bräse*

The pursuit of developing novel approaches to fully organic and efficient phosphorescent materials is in high demand. The optical activity of such functional, organic phosphorescent/fluorescent materials may exhibit great temperature dependence, allowing their application as advanced, highly sensitive molecular thermometers. In this study, a rational strategy involving host–guest complexation and polymerization of [2.2]paracyclophane (PCP) based molecules with cucurbit[8]uril (CB8) to suppress the molecular motion and promote temperature-dependent phosphorescence is presented. The rigid cavity of CB8 provides an ideal microenvironment to host PCP molecules 1 and 2, significantly enhancing the photophysical performance after complexation. Co-polymerizing phosphors 1 and 2 with acrylamide is an efficient method for improving phosphorescence. Incorporating CB8 into the resulting P-1 and P-2 polymers enhances phosphorescence performance. Importantly, the obtained materials exhibit a big structure-dependent spectral shift and change of phosphorescence lifetimes with temperature, allowing novel, phosphorescence-based, and purely organic optical thermometers to be developed. The practical applications of PCP-based luminescent materials in temperature sensing via a multi-parameter approach are showcased, i.e., using fluorescence spectral shift and changes in bandwidth, as well as phosphorescence lifetimes, exhibiting thermal sensitivity of ≈ 17.7 cm^{-1} °C^{-1}, 47.8 cm^{-1} °C, and 5.2% °C^{-1}, respectively.

1. Introduction

Temperature detection is a basic and crucial technique in scientific and industrial fields and our daily lives. With the fast development of optical (luminescence) thermometry, many promising results were reported, benefiting the development of aerospace technology, biomedicine, superconductors, polar explorations, etc.[1–6] Luminescent temperature sensors mainly encompass inorganic materials and nanoparticles, such as Ln$^{3+/2+}$-doped structures, materials based on d-block metal ions, and quantum dots. However, there is a growing interest in soft organic-based luminescent thermometers such as organic dyes, polymers, metal–organic-frameworks (MOF), other organic–inorganic hybrids, and composite structures.[6–8] In general, the benefits of optical organic thermometers are their great susceptibility to temperature changes, high luminescence quantum yield, and brightness, as well as the possibility of advanced and specific modification of their structure according to the requirements of given applications.

X. Qiu, S. Bräse
Institute of Organic Chemistry (IOC)
Karlsruhe Institute of Technology (KIT)
Kaiserstrasse 12, 76131 Karlsruhe, Germany
E-mail: braese@kit.edu
T. Zheng
School of Information and Electrical Engineering
Hangzhou City University
Hangzhou 310015, China
E-mail: zhengteng@zucc.edu.cn

The ORCID identification number(s) for the author(s) of this article can be found under https://doi.org/10.1002/adfm.202313517

M. Runowski, P. Woźny, K. Soler-Carracedo
Faculty of Chemistry
Adam Mickiewicz University
Uniwersytetu Poznańskiego 8, Poznań 61-614, Poland
E-mail: runowski@amu.edu.pl

I. R. Martín, C. E. Piñero
Departamento de Física
IUdEA
IMN and MALTA Consolider Team
Universidad de La Laguna
San Cristóbal de La Laguna, Santa Cruz de Tenerife E-38200, Spain

S. Lebedkin, O. Fuhr
Institute of Nanotechnology (INT)
Karlsruhe Institute of Technology (KIT)
Kaiserstrasse 12, 76131 Karlsruhe, Germany

ADVANCED
SCIENCE NEWS

www.advancedsciencenews.com

ADVANCED
FUNCTIONAL
MATERIALS

www.afm-journal.de

This permits, e.g., selective binding of the given molecules with appropriate targeted biological structures, allowing localized and remote thermal imaging.[9–11] Organic molecular thermometers, which are based on temperature-responsive fluorescent materials, enabling fast photophysical response, outstanding spatial and temporal resolution, good biocompatibility, and high sensitivity, are regarded as one of the most valuable thermometric tools in the cryogenic range. However, designing and developing novel optical thermometers with high sensitivity is still challenging. An efficient strategy to significantly improve the thermal sensitivity of optical sensors may be to exploit the thermal response of the lifetime of phosphorescence in organic phosphor compounds, which may be extremely long for phosphorescence (up to hundreds of milliseconds or even seconds) and highly sensitive to temperature changes. Note that fluorescence phenomena, on the other hand, are very fast, lasting typically in the range of a few nanoseconds. This is due to fluorescence typically originating from allowed singlet–singlet (S_1–S_0) transitions,[12–14] whereas phosphorescence is related to the forbidden triplet–singlet (T_1–S_0) transitions.[15,16] Another promising strategy is to use the spectral shift of the emission bands as a thermometric parameter, which is typically much more susceptible to temperature changes in the case of organic compounds compared with inorganic materials.

Advances in highly efficient and stable room-temperature phosphorescence materials have attracted considerable attention in various fields, such as display technology,[17–19] optoelectronics,[19] optical sensors technology,[20–22] etc.[23,24] This is due to the advantages of organic phosphorescent materials, such as facile modification, biocompatibility, very long emission lifetime, large Stokes shifts, rich triplet states, as well as high quantum yield and brightness, which are not fully covered in fluorescent materials.[25] To improve phosphorescence by enhancing the intersystem crossing (ISC) rate between the excited singlet and triplet states, two main strategies have been proposed: I) introducing heavy atoms to promote spin-orbit coupling and reducing the splitting energy of the S_1 and T_1 states (ΔE_{ST}); II) suppression of the undesired nonradiative transitions from the triplet state by restraining the molecular motions, e.g. by crystallization, polymerization, H-aggregation (molecular self-assembly), and host–guest interaction.[24]

[2.2]Paracyclophane (PCP) is a compact molecule with two slightly curved benzene decks constrained by ethylene bridges in a coplanar conformation. With the short deck distance of 3.09 Å, smaller than the van der Waals distance between the layers of graphite (3.35 Å), strong transannular electronic communication between the benzene decks can occur. PCP-based molecules have been successfully exploited in material science to develop organic light-emitting diodes (OLEDs) and nonlinear

O. Fuhr
Karlsruhe Nano Micro Facility (KNMFi)
Karlsruhe Institute of Technology (KIT)
Kaiserstrasse 12, 76131 Karlsruhe, Germany

S. Bräse
Institute of Biological and Chemical Systems—Functional Molecular Systems (IBCS-FMS)
Karlsruhe Institute of Technology (KIT)
Kaiserstrasse 12, 76131 Karlsruhe, Germany

optical materials.[26,27] However, PCP-based phosphorescent materials were rarely reported in the literature.[28]

To construct a PCP-based phosphorescent thermometer, the supramolecular host–guest assembly provides an alternative approach, wherein phosphor motion can be restrained, and phosphorescence quenching by oxygen can be prevented, thus promoting the phosphorescence phenomenon even at relatively high temperatures.[29] In this study, we utilized cucurbit[8]uril (CB8), a rigid macrocyclic host synthesized by polymerization of glycoluril and formaldehyde as such a host. Additionally, by copolymerizing PCP phosphors with acrylamide, phosphorescence properties were also improved. Furthermore, the polymerized phosphor molecules can be again encapsulated within the CB8 cavities, further enhancing the phosphorescence effect. Finally, we demonstrated the potential application of the encapsulated PCP-based organic fluorophores for optical temperature detection, which may culminate in a new approach for producing novel phosphorescent–fluorescent thermometers. The developed molecular optical thermometers allow multiple-parameter temperature sensing, i.e., detection based on several parameters, including emission spectral position, FWHM, and lifetime, with a relatively high sensitivity of $\approx$17.7 cm^{-1} °C^{-1}, 47.8 cm^{-1} °C^{-1}, and 5.2% °C^{-1}, respectively.
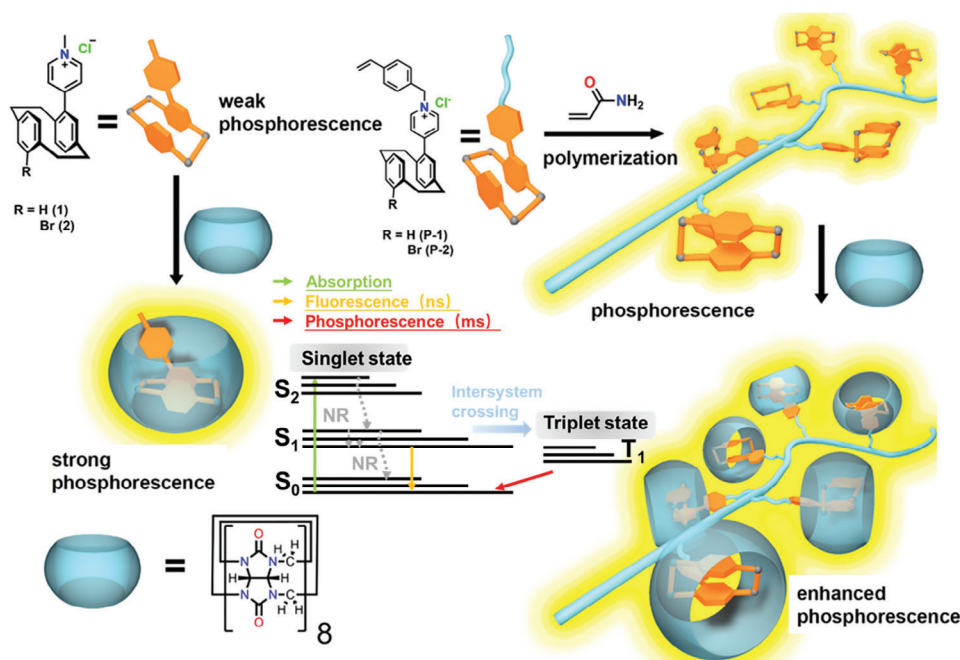
2. Results and Discussion

2.1. Design and Strategy

We have previously reported that CB8 is an ideal host to accommodate methyl-pyridinium-paracyclophane iodide (MPCP-I) in aqueous media complementarily.[30] However, iodide counter ion usually weakens the photophysical performance due to the charge transfer in pyridinium iodides.[31] Therefore, methyl-pyridinium-paracyclophane chloride (sample **1**) was synthesized to access a better photophysical performance (Figures S1–S3, Supporting Information). To investigate the heavy atom effect, which can also influence the photophysical properties, methyl-bromo-pyridinium-paracyclophane chloride (sample **2**) was designed, synthesized, and fully characterized (Figures S6–S8, Supporting Information). On the one hand, encapsulation of the PCP chromophores in the CB8 cavity restrains the molecular motions, promoting the ISC from excited singlet (S1) to triplet (T1) state and reducing the nonradiative decay channels. On the other hand, the rigid shell of the CB8 protects it from the diffusion of molecular oxygen and other possible triplet-state quenchers. Moreover, polymerizing PCP chromophores into a more rigid structure may promote overall phosphorescence performance. In the same fashion, introducing the CB8 host to the PCP polymer may bring a further positive effect on the phosphorescence. **Figure 1** depicts the synthesis, encapsulation, polymerization scheme, and expected phosphorescence enhancement effects. Please note that the detailed mechanism in the materials requires a systematic, complicated study. Thus, here we present the simplified, general energy level diagram for the organic fluorophores studied (Figure 1), highlighting the ground and excited singlet and triplet states, photo-excitation from the ground S_0 to the excited S_1 state, fluorescence, energy transfer from the excited singlet (S_1) to triplet (T_1) state, and finally phosphorescence from the excited T_1 to the ground S_0 state.

2313517 (2 of 13)

**ADVANCED
SCIENCE NEWS**

www.advancedsciencenews.com

**ADVANCED
FUNCTIONAL
MATERIALS**

www.afm-journal.de

Figure 1. The scheme shows the synthesis strategies to boost the phosphorescence phenomena, utilizing encapsulation of the PCP-based materials in the CB8 and their polymerization. The inset shows the scheme of the simplified, general energy level diagram of the phosphorescence and fluorescence.

## 2.2. Host–Guest Interactions of PCP Chromophores with CB8

The binding behavior of the synthesized PCP derivatives (samples **1** and **2**) with CB8 was initially investigated by nuclear magnetic resonance (NMR) spectroscopy. As shown in **Figure** 2a, when an equal molar equivalent of the CB8 was introduced into the sample **1** dissolved in D_2O, the protons from PCP aromatic region (c-i), pyridine (b), and PCP bridge (Figure S11, Supporting Information) were observed significantly upfield shifted, suggesting the deep encapsulation of sample **1** within CB8 cavity. The same phenomenon was also observed for sample **2**, as shown in Figure 2b, where protons b-h and from the PCP bridge (Figure S13, Supporting Information) were upfield shifted. The formation of the 1:1 host–guest complexes was further proved by electrospray ionization (ESI) mass spectrometry in Figures S12 and S14 (Supporting Information), where identical peaks with mass-to-charge ratio (m/z) of 1626.10 for $[1+CB8]^+$ and 1704.75 for $[2+CB8]^+$ were observed.

To gain direct evidence of the complexation of the PCP molecules within the CB8 cavity, a single crystal was obtained by slow evaporation of sample **1** mixed together with CB8 (dissolved in Milli-Q water) and further analyzed by X-ray crystallography (Figure S15 and Table S1, Supporting Information). Due to the disorder of many water molecules non-covalently interacting with the CB8 moiety and the Cl counter ions, their clear identification was hampered. However, the general crystal structure of sample **1** encapsulated in CB8 can be determined, as shown in Figure 2c,d. Indeed, the PCP moiety from molecule **1** is completely stabilized within the CB8 cavity, while the pyridinium part is exposed to the carbonyl portal of the CB8 structure, exhibiting various weak noncovalent bindings (Figure 2c,d), which is consistent with the NMR analysis.

The binding constant for MPCP-I has been reported in our previous study as 3.89 ($\pm$ 0.99) $\times 10^{12}$ M^{-1}.[30] To investigate the binding constant of molecule **2** with CB8, a competitive binding assay was performed utilizing memantine hydrochloride (Mem) as a competitive guest, whose binding constant with CB8 was reported [30] as 8.28 ($\pm$ 0.38) $\times 10^{12}$ M^{-1}. As shown in Figure S16 (Supporting Information), when over one molar equivalent of Mem was introduced to the mixture of compounds **2** and CB8, the proton signals of CB8 from **2**·CB8 and Mem·CB8 were distinctively separated at 5.46 ppm for **2**·CB8 and 5.54 ppm for Mem·CB8. Based on the binding equations, the binding constant of molecule **2** with CB8 was calculated as 1.13 ($\pm$ 0.16) $\times 10^{12}$ M^{-1}, which ensures good stability of the formed complex structure.

2.3. Photophysical Properties of PCP and CB8 Assembly at Ambient Conditions

Further, we studied the photophysical properties of the obtained liquid samples, i.e., **1**, **2**, **1**·CB8, and **2**·CB8 dissolved in aqueous media, as shown in Figures S17–S22 and Table S2 (Supporting Information). Upon the addition of CB8 to sample **1**, the bathochromic-shifted absorption spectra suggest the formation of **1**·CB8 assembly, while the observed photoluminescence (PL) intensity was significantly enhanced (Figure S17, Supporting Information). The luminescence quantum yield (Φ) and fluorescence lifetimes were increased accordingly (Figures S19 and S20, and Table S2, Supporting Information), which was caused by the complexation of molecule **1** with CB8 moiety, promoting the radiative decay (emission) and limiting the nonradiative decay process (see Table S2, Supporting Information). The same behavior
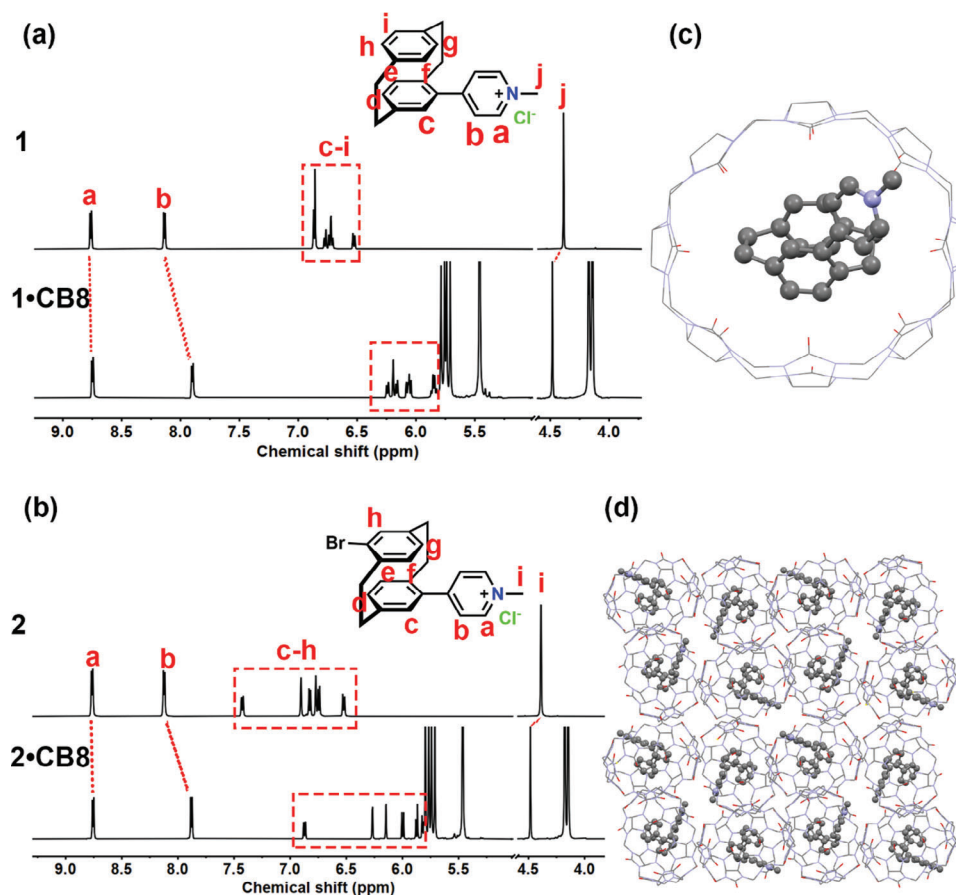
Figure 2. a) ^{1}H NMR spectra (500 MHz, D$_2$O, 298 K) of **1** and **1·CB8** (1:1), the partial region is shown; for full spectra, see Figure S11 (Supporting Information); b) ^{1}H NMR spectra (500 MHz, D$_2$O, 298 K) of **2** and **2·CB8** (1:1), the partial region is shown, for full spectra see Figure S13 (Supporting Information); c) top view of molecular structure of **1·CB8** (from single crystal X-ray diffraction, water molecules were omitted for clarity); d) crystal packing of the **1·CB8** complex (C, gray; N, blue; O, red).

was also found in the case of the complexation of sample **2** with CB8 (Figures S18,S21,S22, and Table S2, Supporting Information).

It has been reported that polymerization could improve the photophysical properties of organic fluorophores by reducing the molecular motions and preventing aggregation-caused quenching processes.[32] Therefore, the polymeric materials **P-1** and **P-2** were designed and synthesized, where the phosphors **1** and **2** were copolymerized with acrylamide (details in Supporting Information). Furthermore, the CB8 compound has been introduced into the **P-1** and **P-2** in aqueous solutions, and the formation of the **P-1·CB8** and **P-2·CB8** complex structures was proved by the NMR studies (Figures S23 and S24, Supporting Information) where the aromatic peaks from the PCP are upfield shifted when the CB8 is introduced to polymers **P-1** and **P-2**. Their photophysical properties were studied and listed in Figures S25–S30 and Table S2 (Supporting Information). Compared to the monochromophores (monomers), polymerization of molecules **1** and **2** greatly enhanced their photophysical properties. The effect of the complexation of chromophores with CB8 is also scaled up in the complex, encapsulated polymer structures **P-1·CB8** and **P-2·CB8**.

Afterward, we investigated in detail the PL performance of the synthesized materials in the solid state, where the effect of water on the chromophores can be minimized. The excitation and emission spectra, luminescence quantum yield, and phosphorescence decay curves were measured to compare the PL properties. As shown in **Figure 3a**, the PL excitation band is located in the range of ≈250–500 nm and dominates in the excitation spectra of all synthesized materials, while the center of the band varies. As shown in Figure 3b, it can be seen that all the emission spectra of the samples are dominated by a broad band located in the range of 370–800 nm, centered ≈500 nm, which is consistent with the emission spectra recorded in the aqueous media. Please note that these observed blue emission bands are associated with the fluorescence of the samples, whereas the phosphorescence bands are bathochromic-shifted to the yellow–orange region, as will be discussed later. As shown in the Commission Internationale de I'Eclairage (CIE) diagram (Figure S31, Supporting Information), different samples show different emission colors, changing from deep blue to green.

Moreover, the luminescence quantum yield (QY) values for all synthesized materials are shown in Figure 3c. In comparison,
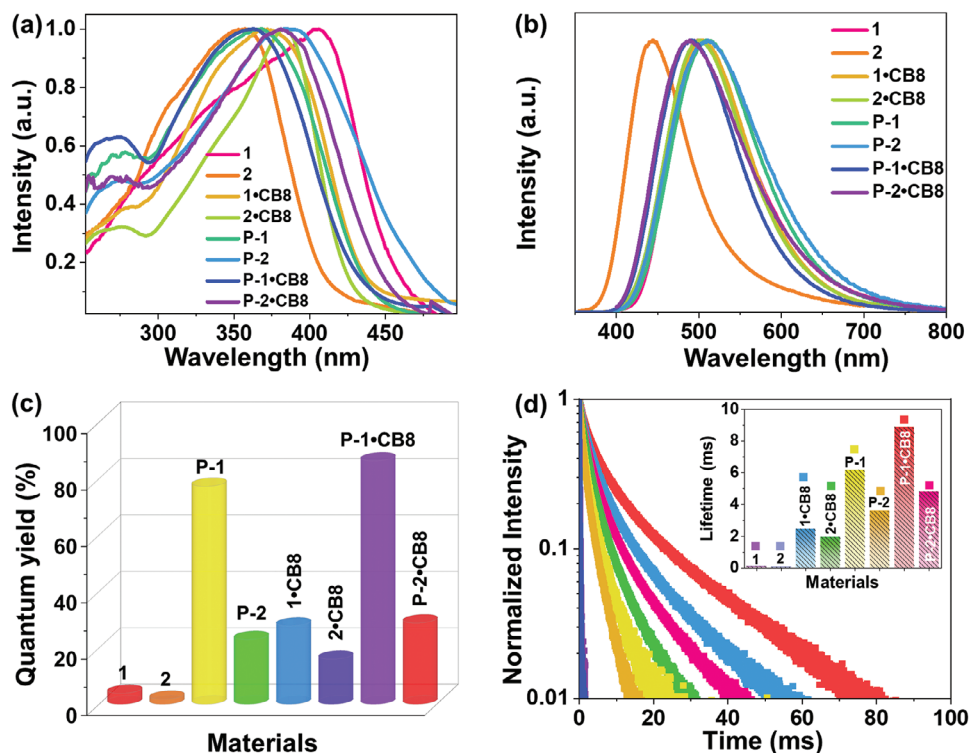
Figure 3. a) Excitation spectra of the materials **1**, **2**, **1**·CB8, **2**·CB8, **P-1**, **P-2**, **P-1**·CB8, and **P-2**·CB8 in solid state form; b) Emission spectra of the corresponding samples; c) Luminescence QY values of the synthesized compounds materials in solid state; d) Phosphorescence decay curves and the determined emission lifetimes (inset) for the developed materials in solid state.

the encapsulation of the CB8 cavity and polymerization of the chromophores can largely improve the QY values of the samples. Using sample 1 as an example (QY = 3.87%), sample 1·CB8 (QY of 27.7%) is ≈7.2 times higher than sample **1**, indicating that the encapsulation of the CB8 cavity significantly elevated QY. Second, **P-1** (QY = 77.3%) shows ≈20 times higher QY than sample **1**, i.e., polymerization of the chromophores also provides the additional possibility to increase the QY value and improve the PL performance. Noteworthy, **P-1**·CB8 presents a very high QY of 86.3%, which greatly improved the QY (≈22 times) compared to sample **1**. On the other hand, in the series of sample **2**, the same QY enhancement effect can also be observed. Namely, in the case of the **P-2** (QY = 22.9%), the polymerization of the chromophores results in ≈13.5 times higher QY than sample **2** (QY = 1.79%). Whereas the QY of sample **2**·CB8 (QY of 16.0%) is ≈8.9 times higher than sample **2**, the complex, encapsulated polymer structure **P-2**·CB8 exhibits QY of 28.8%, which is ≈16 times higher than sample **2**. Such results indicate that encapsulating PCP organic chromophores in the CB8 cavity and their co-polymerization with acrylamide can tremendously boost the QY values.
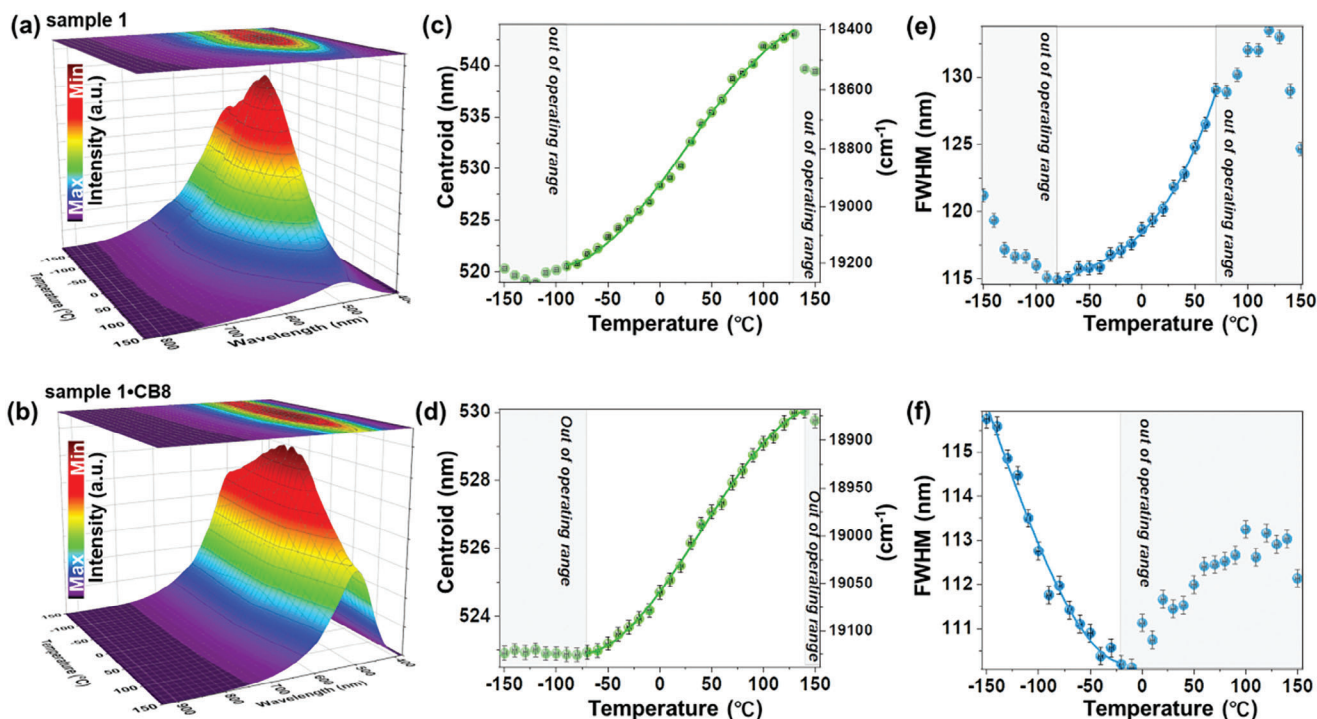
To explore the influence of the encapsulation in the CB8 cavity and polymerization of the PCP chromophores, the measured phosphorescence decay curves and the determined phosphorescence lifetimes are illustrated in Figure 3d and the corresponding inset. As shown, the determined phosphorescence lifetimes at room temperature for the samples **1**, **2**, **P-1**, **P-2**, **1**·CB8, **2**·CB8, **P-1**·CB8, and **P-2**·CB8 are 0.13, 0.08, 6.17, 3.61, 2.46, 1.98, 8.86,

and 4.83 ms, respectively, so in extreme situations they differ by 2-orders of magnitude. The influence of the encapsulation in the CB8 cavity and polymerization of the PCP chromophores on the PL QY is similar to that of the PL lifetime. In other words, the encapsulation and polymerization can largely prolong the PL lifetime, e.g., in sample **2** with **2**·CB8, the emission lifetime was prolonged ≈25 times; for sample **P-2** (polymer), the PL lifetime was prolonged ≈45 times, compared to sample **2** (monomer); from sample **2** to sample **P-2**·CB8, the lifetime was prolonged 60 times (Table S3, Supporting Information). The increase in the lifetime is thus correlated with the increase in QY (see above). The results suggest that the encapsulation in the CB8 cavity and polymerization of the organic chromophores can suppress nonradiative electronic relaxation channels and thus enhance the QY and lifetime. This is probably due to the spatial confinement/restriction of the guest molecules (**1** and **2**) by the CB8 cavity, which largely suppresses molecular motions (vibrations, rotations, and inter-collisions).

2.4. Band-Shift-Based Optical Thermometric Properties

2.4.1. Red-Shift-Based thermometry

To investigate the temperature detection properties of the obtained PCP materials, we first studied the thermostability by thermogravimetric analysis (TGA). The results (Figure S32, Supporting Information) suggested the PCP materials are relatively

**ADVANCED
SCIENCE NEWS**

www.advancedsciencenews.com

**ADVANCED
FUNCTIONAL
MATERIALS**

www.afm-journal.de

Figure 4. a, b) The emission spectra of the selected samples, i.e., **1** and **1**·CB8, as a function of temperature. c, d) The determined $\lambda_{centroid}$ of the emission band as a function of temperature for the samples **1** and **1**·CB8. e, f) The FWHM of the emission band was determined as a function of temperature for samples **1** and **1**·CB8.

stable below 200 °C. After this, the PL properties of all the synthesized samples, from cryogenic temperature to high temperature, were measured. Please note, for optimizing the thermometric performance, we selected the operating temperature range, where the $\lambda_{centroid}$ or FWHM presents only the monotonic change, which is crucial in optical sensing applications. To determine the temperature-dependent spectroscopic parameters and the related thermometric performances, the corresponding spectra were converted to the energy scale using the Jacobian transformation,[33] minimizing the quantitative error of the emission spectra analysis. As disclosed in **Figure** 4a,b, the intensity of sample **1** increases with a temperature below −70 °C; after that, it shows a declining trend with further elevating the temperature. For sample **1**·CB8, it exhibits a similar tendency, and the emission spectra' highest intensity appeared at 10 °C. In the selected temperature range, which can be accessed for optical thermometry, samples 1 and 1·CB8 emission bands show significant spectral redshift (toward lower energy) with temperature rising. As shown in Figure 4c–f, to study the optical thermometric properties, the determined band centroid ($\lambda_{centroid}$) and bandwidth (fullwidth half maximal; FWHM) of sample **1** and **1**·CB8 can be fitted to third-order polynomial functions in a relatively broad temperature range, i.e.

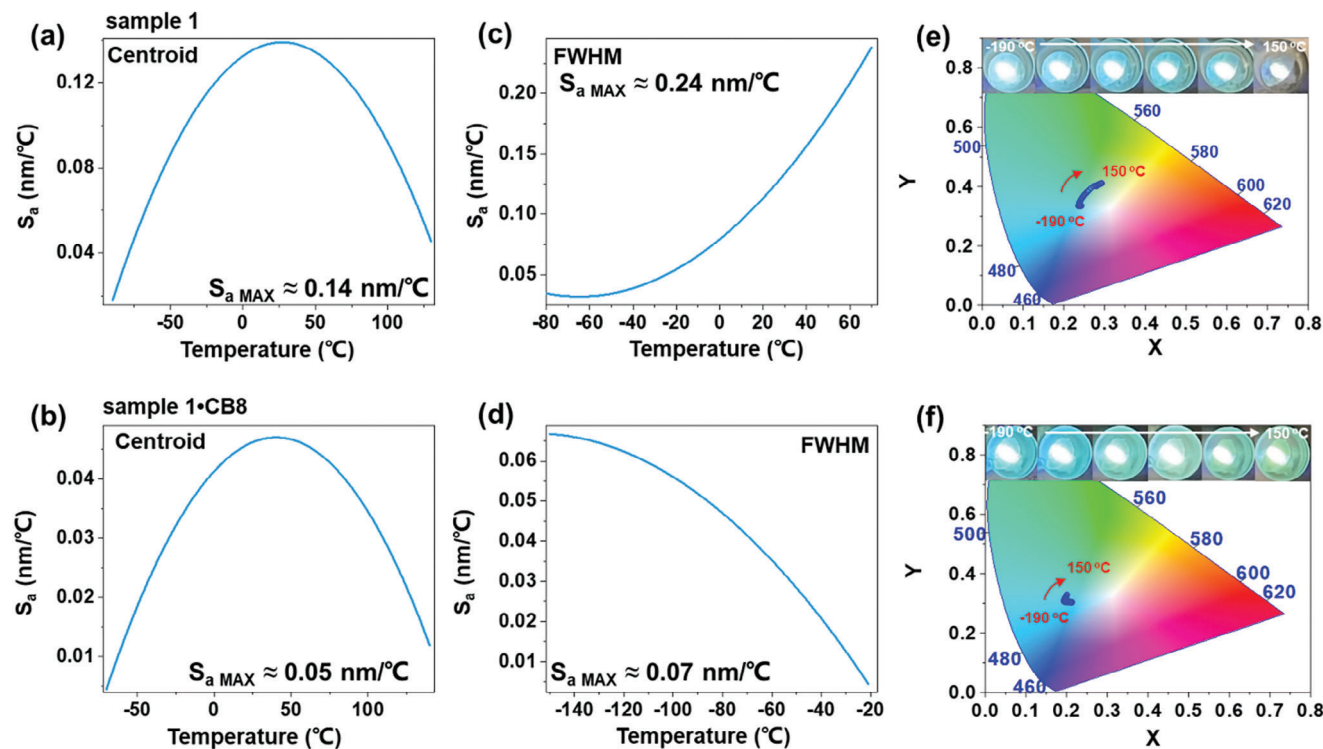$$\lambda_{centroid} \ (or \ FWHM) \ = A_3 \ T^3 + A_2 T^2 + A_1 T + A_0 \qquad (1)$$

where A_0, A_1, A_2, and A_3 are constants and T is temperature. Please note that the fitting function for other samples is also third or fourth polynomial function to analyze the thermometric properties. Herein, these fitting constants are shown in Table S4 (Sup-

porting Information). In the case of sample **1** (see Figure 4c,e), the $\lambda_{centroid}$ increases from 520.6 nm at −90 °C to 543.0 nm at 130 °C with a monotonic shift of 22.4 nm ($\approx$−708.5 cm^{-1}). FWHM changed from 114.9 nm at −80 °C to 129.0 nm at 70 °C, with a band-broadening of 14.1 nm (239.7 cm^{-1}). On the other hand, for sample **1**·CB8, the $\lambda_{centroid}$ increases from 522.9 nm at −70 °C to 530.0 nm at 140 °C, leading to a spectral shift of 7.1 nm ($\approx$−283.4 cm^{-1}). The FWHM decreases from 115.8 nm at −150 °C to 111.7 nm at 20 °C, leading to a total decrease in FWHM of 4.1 nm, i.e., $\approx$−296.3 cm^{-1}.

Thermal sensitivity is the rate of change of the thermometric parameter in response to the temperature variation. To quantitatively investigate the performances of the developed PCP materials for temperature sensing, the absolute sensitivity, i.e., S_a, is estimated using the following functions:

$$S_a = \left| \frac{d\lambda_{centroid}}{dT} \right| \ or \ \left| \frac{dFWHM}{dT} \right| \qquad (2)$$

The S_a curves based on $\lambda_{centroid}$ and FWHM versus temperature of samples **1** and **1**·CB8 are shown in **Figure** 5a–d, respectively. The $S_{a \ MAX}$ based on $\lambda_{centroid}$ and FWHM of samples **1** are 4.37, 6.51 cm^{-1} °C^{-1}, i.e., 0.14 and 0.24 nm °C^{-1}, respectively. Those of sample **1**·CB8 are 1.71 cm^{-1} °C^{-1} (0.05 nm °C^{-1}) and 3.02 cm^{-1} °C^{-1} (0.07 nm °C^{-1}), respectively. It can also be seen that the temperature-dependent color of both samples is slightly changed from cold cyan to warm cyan (see Figure 5c,f). Importantly, in the selected temperature ranges, the emission bands of 1 and 1·CB8 demonstrate a significant redshift, indicating their potential in optical thermometry.

**ADVANCED
SCIENCE NEWS**

www.advancedsciencenews.com

**ADVANCED
FUNCTIONAL
MATERIALS**

www.afm-journal.de

Figure 5. a, b) The absolute temperature sensitivity (Sa) was determined based on the $\lambda_{centroid}$ of samples **1** and **1**·CB8. c, d) The S$_a$ is based on the FWHM of samples **1** and **1**·CB8. f) The digital photographs of samples **1** and **1**·CB8 under UV excitation as a function of temperature.
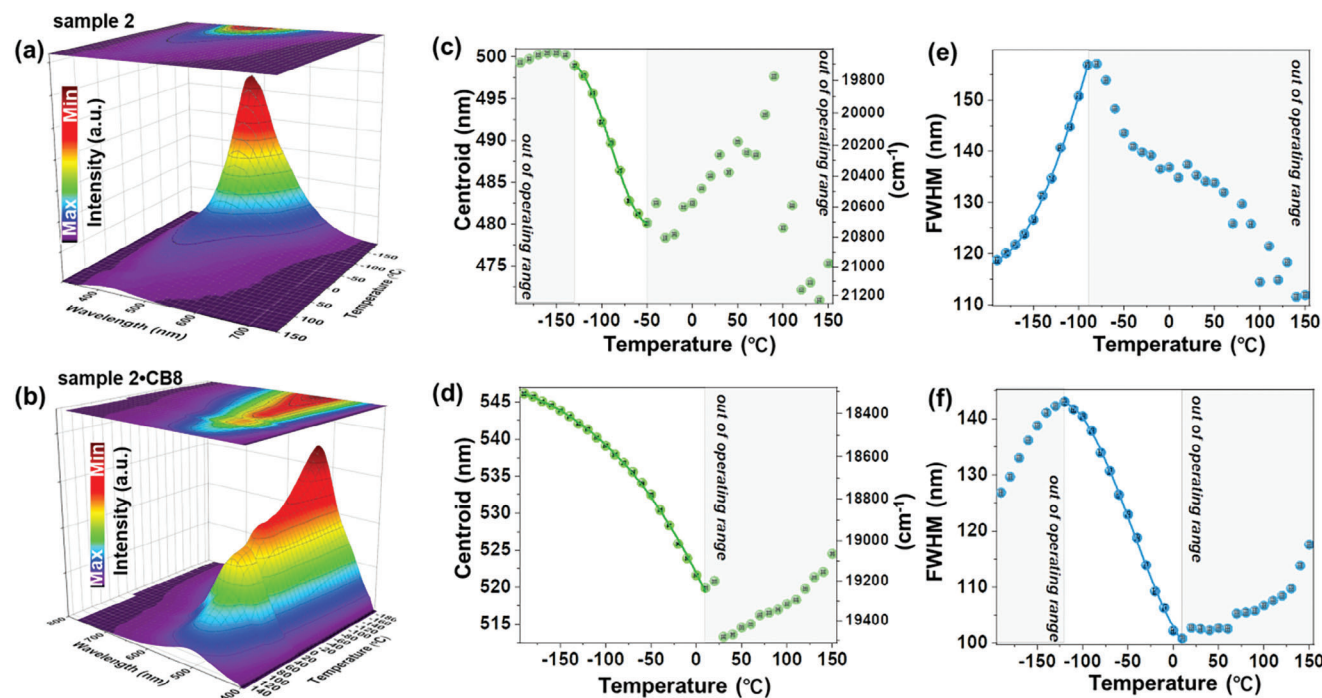
2.4.2. Blue-Shift-Based Thermometry

To investigate the temperature-sensing properties of other synthesized PCP samples, the emission spectra of samples **2** and **2**·CB8 at various temperatures are recorded, and corresponding temperature-sensing performances are illustrated in **Figures 6** and **Figure 7**. The emission bands of samples **2** and **2**·CB8 show significant spectral blue-shift (toward higher energy) with rising temperatures, opposite to samples **1** and **1**·CB8. As shown in Figure 6a,b, the intensity of the emission band of sample **2** shows a monotonically decline tendency with increasing temperature. Meanwhile, sample **2**·CB8 exhibits a decreasing tendency but a much lower rate, which is beneficial for optical sensing. The thermometric properties based on $\lambda_{centroid}$ and FWHM of samples **2** and **2**·CB8 were studied in detail, shown in Figure 4c–f. In the selected temperature range, the $\lambda_{centroid}$ of sample **2** blue-shifts from 499.0 nm at −130 °C to 480.1 nm at −50 °C (total shift of −18.9 nm, i.e., 1046.1 cm^{-1}), while FWHM increases from 118.8 nm at −190 °C to 156.9 nm at −90 °C (total FWHM change of 38.1 nm, i.e., 1950.6 cm^{-1}).

On the other hand, the $\lambda_{centroid}$ of sample **2**·CB8 exhibits a blue shift from 546.2 nm at −190 °C to 519.9 nm at 10 °C, i.e., a total shift of −26.3 nm (744.1 cm^{-1}). The FWHM change from 143.0 nm at −120 °C to 100.9 nm at 10 °C, that is, total FWHM change of 42.1 nm, i.e., −1301.8 cm^{-1}. The temperature-dependent $\lambda_{centroid}$ or FWHM of samples **2** and **2**·CB8 can be well fitted to polynomial function (third or fourth order) in the selected temperature range to study the thermometric properties. As mentioned before, the restriction of the guest molecules by CB8 largely suppresses the molecular motions, and the CB8

cage can shield the triplet states and the guest molecules from quenchers, thus weakening the thermal response of the optical properties of developed samples. It is clear that the luminescence properties of the "bare" molecule, i.e., sample **2**, are more susceptible to temperature changes; however, the optical thermometer having the molecular "cage," i.e., sample **2**·CB8 shows monotonic changes in broader T-range, it has better QY and high intensity, still having a satisfactory thermal response.

The temperature sensing performances as a function of the temperature of samples **2** and **2**·CB8 are illustrated in Figure 7a–f. In the case of sample **2**, the S$_a$ value based on $\lambda_{centroid}$ initially shows an increasing tendency, reaching the optimal S$_a$ (S$_{a\,MAX}$) of 0.33 nm °C^{-1} (≈17.7 cm^{-1} °C^{-1}) at −90 °C, and then a decreasing trend is observed with further temperature elevation (see Figure 7a). The S$_a$ value based on FWHM demonstrates a monotonically increasing tendency, achieving the maximal value of 0.61 nm °C^{-1} (≈47.8 cm^{-1} °C^{-1}) at −90 °C (see Figure 7c). Please note that such a large shift rate is one of the highest compared to the previously described organic or inorganic optical thermometer based on spectral band shift, which will be discussed in the following paragraph. Interestingly, the emission color of the UV-irradiated sample demonstrates a significant visual color-tuning with increasing temperature, changing from yellow to green, then to cyan, and finally to deep blue, as shown in Figure 7e. For the sample **2**·CB8 (see Figure 7b,d,f), it is clear that the S$_a$ based on $\lambda_{centroid}$ shows a continuously increasing trend with temperature rising, reaching 0.26 nm °C^{-1} (6.4 cm^{-1} °C^{-1}) of the S$_{a\,MAX}$, while the S$_a$ based on FWHM shows a maximum of 0.43 nm °C^{-1} (13.8 cm^{-1} °C^{-1}) at −45 °C. The emission color of the sample **2**·CB8 is tuned from yellowish green to cyan, then

**ADVANCED
SCIENCE NEWS**

www.advancedsciencenews.com

**ADVANCED
FUNCTIONAL
MATERIALS**

www.afm-journal.de

Figure 6. a, b) The emission spectra of the selected samples, i.e., **2** and **2·CB8**, as a function of temperature. c, d) The determined $\lambda_{centroid}$ of the emission band and the determined FWHM of the band as a function of temperature for samples **2** and **2·CB8**, respectively.
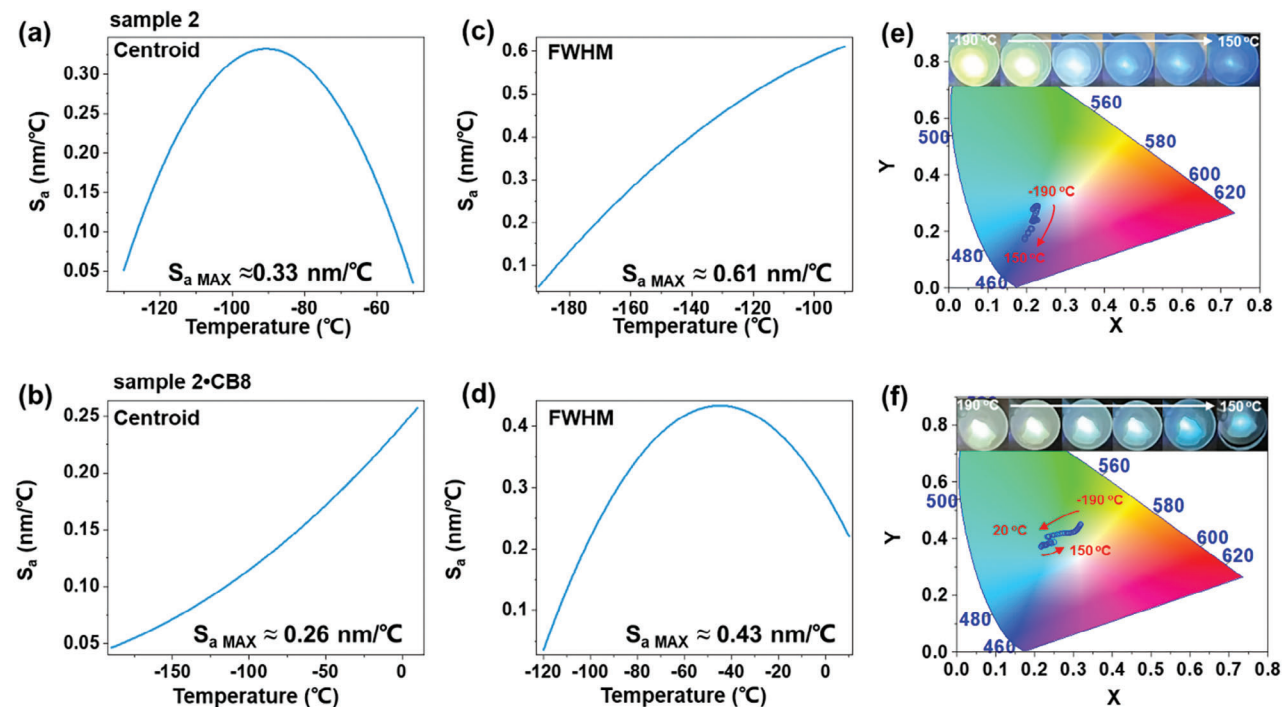
Figure 7. a, b) The determined absolute temperature sensitivity (S_a) based on the $\lambda_{centroid}$ of the samples **2** and **2·CB8**. c, d) The S_a is based on the FWHM of samples **2** and **2·CB8**. f) The digital photographs of samples **2** and **2·CB8** under UV light as a function of temperature.

**ADVANCED
SCIENCE NEWS**

www.advancedsciencenews.com

**ADVANCED
FUNCTIONAL
MATERIALS**

www.afm-journal.de

finally to deep cyan with temperature increases from −190 °C to 150 °C (Figure 7f). Importantly, the measurable temperature ranges of samples **2** and **2·CB8** are located in the cryogenic range (down to −190 °C), indicating that these two samples can be applied as highly sensitive temperature sensing materials in the cryogenic range.

A detailed explanation of a mechanism governing the observed structure-dependent red- and blue-shifts of the emission bands is beyond this work's scope and requires further investigations, including complex theoretical calculations. However, here we note that the observed redshift (for the compounds without heavy atoms) is caused by the decreasing energy difference between the ground and excited (emitting) states, whereas the blue-shift (for the compounds with heavy atoms) implies an increase of that energy gap with temperature. Please note that the temperature-induced spectral shifts in materials are often associated with their unit cell expansion with temperature or, more rarely, contraction in the case of structures with a negative thermal expansion coefficient (static contributions). On the other hand, the temperature elevation enhances electron–phonon interactions (vibrational contribution), as well as intra- and intermolecular interaction, which may contribute to the observed spectral shifts and changes in the width of the emission bands with temperature, making the whole mechanism even more complex for the organic compounds studied.

Moreover, in our case, the presence of heavy atoms, which in general should promote the spin-orbit coupling of the phosphorescent molecules, resulted in a sight deterioration of their phosphorescence performance, including emission lifetimes and quantum yields. It may be associated with competing charge transfer processes in pyridinium bromides, similarly as in the case of iodide counter ions, which typically weakens the phosphorescence performance of various organic materials. For comparison, the temperature sensing performances of all obtained samples are summarized in **Table 1**. Please note that the temperature sensing performances of the samples **P-1**, **P-1·CB8**, **P-2**, and **P-2·CB8** are presented in Figure S33–S36 (Supporting Information). It is shown that the $S_{a\,MAX}$ values obtained for samples **1** and **2** are 6.51 and 47.8 cm^{-1} °C^{-1}, which are much higher than the ones for the samples **P-1** and **P-2**, i.e., 4.82 and 2.59 cm^{-1} °C^{-1}, respectively, indicating that the polymerization of the chromophores leads to smaller susceptibility to temperature changes. In general, the bare molecules, i.e., samples **1** and **2**, present a higher thermal sensitivity than the **1·CB8** and **2·CB8** ones, respectively, confirming that the encapsulation in the CB8 cavity restricts the molecular motions of the organic molecules studied, and the CB8 can shield the triplet states of the guest chromophores from exposing directly to the stimulus of the external environment, thus slightly weaken their thermal response. However, as was already mentioned, the luminescent thermometers with molecular "cage" exhibit monotonic changes in the broader T-range; they have significantly better QY and much higher signal intensity. Hence, these benefits compensate very well for a bit smaller sensitivity and indicate that materials with molecular cages are much better and reasonable choices for their implementation as optical thermometers. Such multi-parameter thermometers can avoid potential biases in temperature detection in case of possible spectral interferences, which is common in real temperature sensing applications.

Table 1. The temperature sensing performances, i.e., $S_{a\,MAX}$, T, and T-range, based on $\lambda_{centroid}$ and FWHM of the different obtained samples.
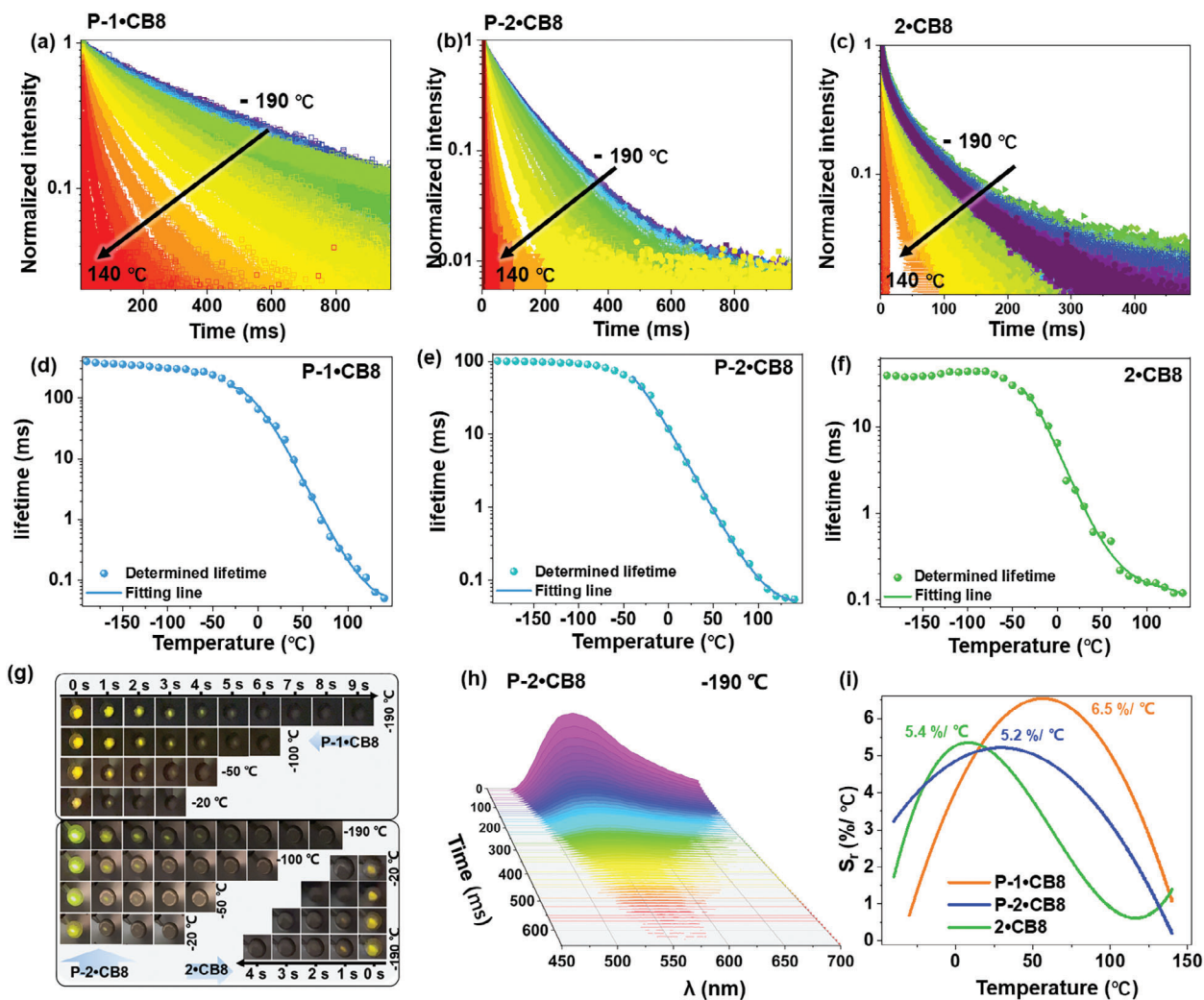
Sample		$S_{a\,MAX}$ [cm^{-1} °C^{-1}]	$S_{a\,MAX}$ [nm °C^{-1}]	T [°C]	T-range [°C]
1	$\lambda_{centroid}$	4.37	0.14	12	−90–130
	FWHM	6.51	0.24	70	−80–70
2	$\lambda_{centroid}$	17.7	0.33	−95	−130 to −50
	FWHM	47.8	0.61	−90	−190 to −90
P-1	$\lambda_{centroid}$	1.16	0.07	−31	−60–10
	FWHM	4.82	0.14	−9	−110–10
P-2	$\lambda_{centroid}$	1.50	0.06	120	−80–120
	FWHM	2.59	0.11	140	−70–140
1·CB8	$\lambda_{centroid}$	1.71	0.05	−7	−70–140
	FWHM	3.02	0.07	−126	−150 to −20
2·CB8	$\lambda_{centroid}$	6.4	0.26	10	−190–10
	FWHM	13.8	0.43	−44	−120–10
P-1·CB8	$\lambda_{centroid}$	1.07	0.08	10	−190–10
	FWHM	6.1	0.14	−24	−150–20
P-2·CB8	$\lambda_{centroid}$	5.4	0.03	−2	−190 – −70
	FWHM	5.2	0.02	−7	−190 to −50

2.5. Lifetime-Based Optical Thermometry

To explore the temperature sensing properties based on the emission lifetime, the temperature-dependent phosphorescence decay curves of the selected samples with superior QY, i.e., **2·CB8**, **P-1·CB8** and **P-2·CB8**, were measured in the broad temperature range (from −190 to 140 °C) and presented in **Figure 8a–c**. Phosphorescence was chosen over fluorescence in this case due to the long-lasting nature of phosphorescence facilitating its applications for optical temperature sensing. The emission decay curves of the samples at low temperatures (see Figure 8d) are very long. That is why, for the **P-1·CB8** sample at the lowest temperature values (where the phosphorescence lasted extremely long), due to technical limitations, the decay curves seem to be cut at ≈1 s (Figure 8a). Nonetheless, we have used the following expression to give an estimation of the average lifetimes:

$$\langle \tau \rangle = \frac{\int_0^\infty I(t)\,dt}{I(0)} \qquad (3)$$

where $I(t)$ is the acquired intensity as a function of the time. As shown in Figure 8a–c, the phosphorescence decay curves of all samples show strong temperature dependence, and the corresponding lifetimes monotonically shorten with increasing temperature. This shortening is due to the well-established thermal quenching processing, including the enhanced nonradiative relaxation probability with temperature, increased fluorescence probability concerning the competing phosphorescence phenomenon, back-energy transfer, improved electron–phonon coupling, etc. Initially, the determined lifetimes shorten slowly in the temperature range from −190 to −50 °C, but afterward, till ≈140 °C, their values decrease at much higher rates (see Figure 8d–f). The determined phosphorescence lifetimes as a function of temperature, selected in the range of the biggest

ADVANCED
SCIENCE NEWS

www.advancedsciencenews.com

ADVANCED
FUNCTIONAL
MATERIALS

www.afm-journal.de

Figure 8. a, c) The phosphorescence decay curves for the selected samples, i.e., **2**·CB8, **P-1**·CB8 and **P-2**·CB8, recorded in temperature range from −190 to 140 °C. d, f) The determined phosphorescence lifetimes as a function of temperature for the corresponding samples. g) Digital photographs showing time-resolved phosphorescence (after UV exposure; laser off) of the selected samples as different temperature values. h) The representative time-resolved emission spectra of the sample **P-2**·CB8 measured at −190 °C. i) The determined relative sensitivity (S_r) values as a function of temperature.

and most monotonic change, can be well-fitted to a third- or fourth-order polynomial function. The fitting parameters are shown in Table S4 (Supporting Information). The digital photographs of the phosphorescence of the selected samples as a function of time are presented in Figure 8g. The corresponding time-resolved phosphorescence spectra of the representative sample **P-2**·CB8 as a function of time at −190 °C are presented in Figure 8h. The corresponding time-resolved phosphorescence spectra of **P-1·CB8** and **2·CB8** are also presented in Figure S37 (Supporting Information). Note that the phosphorescence decay seems to be faster in Figure 8h, in contrast to Figure 8g, simply due to a much better time resolution of the measurements (recorded every 10 ms), which comes at the cost of scarifying exposure time, compared to the digital photographs.

In difference to thermometry based on band-shift and FWHM, the most reliable figure of merit for sensing based on the emission lifetimes is relative sensitivity (S_r), which is usually ex-

pressed in % and shows how the measured parameter changes per 1 K of absolute temperature.

$$S_r = \frac{1}{\tau} \times \left| \frac{d\tau}{dT} \right| \times 100\% \tag{4}$$

The corresponding S_r values versus temperature are estimated and illustrated in Figure 8f. The optimal S_r value ($S_{r\,MAX}$) for the samples **P-1**·CB8, **P-2**·CB8, and **2**·CB8 are 6.5% °C^{-1} (at 56 °C), 5.2% °C^{-1} (at 30 °C) and 5.4% °C^{-1} (at 8 °C). The lifetime-based thermometry with the **P-2**·CB8 sample also has a very broad operating temperature range, i.e., from −40 to 140 °C.

Please note that combined with the thermometry mentioned above based on $\lambda_{centroid}$ and FWHM, the developed materials can be used as multi-parameter, remote thermometers, which can realize good thermal sensitivity in the whole measured temperature range, including the cryogenic and high-temperature regions, which overcomes the drawbacks of single-parameter

**ADVANCED
SCIENCE NEWS**

www.advancedsciencenews.com

**ADVANCED
FUNCTIONAL
MATERIALS**

www.afm-journal.de

Table 2. Temperature sensing performances, including maximal sensitivities for different organic and inorganic luminescent thermometers based on the band-shift, FWHM, LIR, and emission lifetimes. Sensitivities marked with asterisks (*) are estimated from figures in the references.

Thermometers	Measured parameter	Maximal Sensitivity [x °C⁻¹]	T [°C]	T-range [°C]	Ref.
Sample 2	band-shift	17.7 cm⁻¹	≈−95	−130 to −50	This work
Sample 2·CB8	band-shift	6.4 cm⁻¹	≈10	−190–10	This work
SrB_4O_7:Tm^{2+}	band-shift	1.44 cm⁻¹	27	−260–27	[34]
LaF_3: Nd/LaF_3	band-shift	0.14 cm⁻¹	30–70	30–70	[35]
$LaPO_4$:Tm^{3+}, Yb^{3+}	band-shift	0.12 cm⁻¹	20–500	20–500	[36]
$Na_4Mg(WO_4)_3$:Mn^{4+}	band-shift	≈2.67 cm⁻¹*	27	−173–127	[37]
YAG: Ce^{3+}	band-shift	−1.19 cm⁻¹	25–185	25–185	[38]
YVO_4:Eu^{3+}	band-shift	0.22 cm⁻¹*	427	−23–427	[39]
Sample 2	FWHM	47.8 cm⁻¹	≈−90	−190 to −90	This work
Sample 2·CB8	FWHM	13.8 cm⁻¹	≈−44	−120–10	This work
SrB_4O_7:Tm^{2+}	FWHM	3.85 cm⁻¹	27	−260–27	[34]
YAG: Ce^{3+}	FWHM	−1.45 cm⁻¹	25–185	25–185	[38]
YVO_4:Dy^{3+}	FWHM	0.11 cm⁻¹	−23–427	−23–427	[39]
$YAlO_3$: Nd^{3+}	FWHM	≈0.21 cm⁻¹*	20–97	20–97	[40]
Sample 2·CB8	lifetime	5.4%	8	−40–140	This work
Sample P-1·CB8	lifetime	6.5%	56	−30–140	This work
Sample P-2·CB8	lifetime	5.2%	30	−10–150	This work
Ru–phen complex	lifetime	2.5%	77	7–52	[41]
NBD–Laurdan	lifetime	1.5%	67	7–67	[42]
C_{70} in PtBMA	lifetime	2.2%	90	20–90	[43]
PNIPAM	lifetime	10.4%	35	20–45	[44]
Fluorescent polymer	lifetime	4.4%	38	23–53	[45]
SrB_4O_7:Tm^{2+}	lifetime	4.16%	64	−260–127	[34]
$KLu(WO_4)_2$: Ho^{3+}, Yb^{3+}	lifetime	0.39%	24	24–400	[46]
YVO_4: Ho^{3+}, Yb^{3+}	lifetime	1.35%	27	−261–27	[47]
La_2O_3: Er^{3+}, Tm^{3+}, Yb^{3+}	lifetime	≈0.67%	25–60	25–60	[48]
$Gd_3Al_5O_{12}$:Mn^{3+}, Mn^{4+}	lifetime	2.08%	−24	−153–297	[49]
$Lu_2(Ge_{0.25}Si_{0.75})O_5$: Pr^{3+}	lifetime	1.45%	7	2–152	[49]
$Li(PO_3)_4$: Pr^{3+}	lifetime	0.62%	90	25–90	[50]
$Na(PO_3)_4$: Pr^{3+}	lifetime	0.59%	90	25–90	[50]
$K(PO_3)_4$: Pr^{3+}	lifetime	0.56%	90	25–90	[50]
PrP_5O_{14}	lifetime	0.46%	90	25–90	[50]
$Bi_2Ga_4O_9$:Cr^{3+}	lifetime	1.35%	227	−263–227	[51]

thermometers. Thermometric performances of the developed molecular temperature sensors, including their sensitivity (S_a for $\lambda_{centroid}$ and FWHM, S_r for a lifetime) and operating temperature range, are compared with other luminescent thermometers in **Table 2**. Compared with other thermometers, the developed organic sensors show 3 approaches for temperature determination, and in each category, they are one of the thermometers with the highest sensitivity. In particular, in the category of FWHM, sample **2** shows a sensitivity of one order of magnitude higher than other reported thermometers. These results indicate the great potential of the developed molecular sensors as superior and super-sensitive, noninvasive optical thermometers.

3. Conclusion

A novel rational strategy related to host–guest complexation, encapsulation, and polymerization of PCP-based molecules with

CB8 organic cage to suppress the molecular motions and promote efficient phosphorescence was studied. The rigid and hydrophobic CB8 cavity provides an ideal microenvironment to host PCP molecules 1 and 2, thus largely improving the photophysical performance after complexation. Moreover, co-polymerizing phosphors 1 and 2 with acrylamide is an efficient method to improve the phosphorescence phenomenon. Incorporating a CB8 molecular cage into the resulting P-1 and P-2 polymers leads to enhanced phosphorescence performance. The designed and synthesized organic phosphors demonstrate superior thermally induced spectral shift, FWHM change, and a huge variation of luminescence lifetimes, developing novel, fluorescence- and phosphorescence-based molecular optical thermometers with great sensitivity. Depending on the material structure and their encapsulation in organic cages, they exhibit either red- or blue-shifts with temperature and bright, yellow phosphorescence lasting several seconds in the cryogenic

**ADVANCED
SCIENCE NEWS**

www.advancedsciencenews.com

**ADVANCED
FUNCTIONAL
MATERIALS**

www.afm-journal.de

T-range. The practical applications of PCP-based phosphorescent materials in temperature sensing were demonstrated via a multi-parameter approach, i.e., spectral-shift, bandwidth, and phosphorescence lifetime, highlighting their high thermal sensitivity of ≈ 17.7 cm^{-1} °C^{-1}, ≈ 47.8 cm^{-1} °C^{-1}, and 5.2% °C^{-1}. Such a strategy allowed to cover a very broad temperature range, including cryogenic and high-temperature regions, i.e., from −190 to 140 °C, which is very beneficial in optical temperature sensing applications.

Supporting Information

Supporting Information is available from the Wiley Online Library or from the author.

Conflict of Interest

The authors declare no conflict of interest.

Data Availability Statement

The data that support the findings of this study are available in the supplementary material of this article.

[1] Y. Gao, Y. Bando, *Nature* **2002**, *415*, 599.

[2] C. D. S. Brites, P. P. Lima, N. J. O. Silva, A. Millán, V. S. Amaral, F. Palacio, L. D. Carlos, *Nanoscale* **2012**, *4*, 4799.

[3] J. Rocha, C. D. S. Brites, L. D. Carlos, *Chem. Eur. J.* **2016**, *22*, 14782.

[4] C. D. S. Brites, S. Balabhadra, L. D. Carlos, *Adv. Opt. Mater.* **2019**, *7*, 1801239.

[5] M. D. Dramićanin, *J. Appl. Phys.* **2020**, *128*, 040902.

[6] M. Runowski, P. Wozny, N. Stopikowska, I. R. Martín, V. Lavín, S. Lis, *ACS Appl. Mater. Interfaces.* **2020**, *12*, 43933.

[7] D. Ananias, A. D. G. Firmino, R. F. Mendes, F. A. A. Paz, M. Nolasco, L. D. Carlos, J. Rocha, *Chem. Mater.* **2017**, *29*, 9547.

[8] V. Trannoy, A. N. Carneiro Neto, C. D. S. Brites, L. D. Carlos, H. Serier-Brault, *Adv. Opt. Mater.* **2021**, *9*, 2001938.

[9] B. Saha, B. Ruidas, S. Mete, C. D. Mukhopadhyay, K. Bauri, P. De, *Chem. Sci.* **2020**, *11*, 141.

[10] H. Ma, T. Zhou, Z. Dai, J. Hu, J. Liu, *Adv. Opt. Mater.* **2019**, *7*, 1900326.

[11] T. Barilero, T. L. Saux, C. Gosse, L. Jullien, *Anal. Chem.* **2009**, *81*, 7988.

[12] W. Zheng, P. Huang, D. Tu, E. Ma, H. Zhu, X. Chen, *Chem. Soc. Rev.* **2015**, *44*, 1379.

[13] Y. Zhou, H. Ming, S. Zhang, T. Deng, E. Song, Q. Zhang, *J. Chem. Eng.* **2021**, *415*, 129448.

[14] A. Patra, C. S. Friend, R. Kapoor, P. N. Prasad, *Chem. Mater.* **2003**, *15*, 3650.

[15] H. Xiang, J. Cheng, X. Ma, X. Zhou, J. J. Chruma, *Chem. Soc. Rev.* **2013**, *42*, 6128.

[16] P. D. Fleischauer, P. Fleischauer, *Chem. Rev.* **1970**, *70*, 199.

[17] R. Kabe, N. Notsuka, K. Yoshida, C. Adachi, *Adv. Mater.* **2016**, *28*, 655.

[18] H. Xu, R. Chen, Q. Sun, W. Lai, Q. Su, W. Huang, X. Liu, *Chem. Soc. Rev.* **2014**, *43*, 3259.

[19] X. Liu, L. Yang, X. Li, L. Zhao, S. Wang, Z. Lu, J. Ding, L. Wang, *Angew. Chem., Int. Ed.* **2021**, *60*, 2455.

[20] D.-A. Xu, Q.-Y. Zhou, X. Dai, X.-K. Ma, Y.-M. Zhang, X. Xu, Y. Liu, *Chin. Chem. Lett.* **2022**, *33*, 851.

[21] L. Zang, W. Shao, M. S. Kwon, Z. Zhang, J. Kim, *Adv. Optical Mater.* **2020**, *8*, 2000654.

[22] J. Li, H. Zhang, Y. Zhang, W. Zhou, Y. Liu, *Adv. Optical Mater.* **2019**, *7*, 1900589.

[23] Z. Zhang, Y. Chen, Y. Liu, *Angew. Chem., Int. Ed.* **2019**, *58*, 6028.

[24] Z.-Y. Zhang, Y. Liu, *Chem. Sci.* **2019**, *10*, 7773.

[25] C. C. Kenry, B. Liu, *Nat. Commun.* **2019**, *10*, 2111.

[26] M. R. Cerón, M. Izquierdo, N. Alegret, J. A. Valdez, A. Rodríguez-Fortea, M. M. Olmstead, A. L. Balch, J. M. Poblet, L. Echegoyen, *Chem. Commun.* **2016**, *52*, 64.

[27] N. Sharma, E. Spuling, C. M. Mattern, W. Li, O. Fuhr, Y. Tsuchiya, C. Adachi, S. Bräse, I. D. W. Samuel, E. Zysman-Colman, *Chem. Sci.* **2019**, *10*, 6689.

[28] X. Liang, T. Liu, Z. Yan, Y. Zhou, J. Su, X. Luo, Z. Wu, Y. Wang, Y. Zheng, J. Zuo, *Angew. Chem., Int. Ed.* **2019**, *58*, 17220.

[29] X.-K. Ma, Y. Liu, *Acc. Chem. Res.* **2021**, *54*, 3403.

[30] M. Serhan, M. Sprowls, D. Jackemeyer, M. Long, I. D. Perez, W. Maret, N. Tao, E. Forzani, presented at AIChE Annual Meeting, Conf. Proc., Orlando, FL, USA, November, **2019**.

[31] E. M. Kosower, J. A. Skorcz, W. M. Schwarz, J. W. Patton, *J. Am. Chem. Soc.* **1960**, *82*, 2188.

[32] Z. Zhang, W. Xu, W. Xu, J. Niu, X. Sun, Y. Liu, *Angew. Chem., Int. Ed.* **2020**, *59*, 18748.

[33] J. Mooney, P. Kambhampati, *J. Phys. Chem. Lett.* **2013**, *4*, 3316.

[34] T. Zheng, M. Sójka, M. Runowski, P. Woźny, S. Lis, E. Zych, *Adv. Optical Mater.* **2021**, *9*, 2101507.

[35] U. Rocha, C. Jacinto Da Silva, W. Ferreira Silva, I. Guedes, A. Benayas, L. Martínez Maestro, M. Acosta Elias, E. Bovero, F. C. J. M. Van Veggel, J. A. García Solé, D. Jaque, *ACS Nano* **2013**, *7*, 1188.

[36] M. Runowski, A. Shyichuk, A. Tymiński, T. Grzyb, V. Lavín, S. Lis, *ACS Appl. Mater. Interfaces.* **2018**, *10*, 17269.

[37] D. K. Amarasinghe, F. A. Rabuffetti, *Chem. Mater.* **2019**, *31*, 10197.

[38] W. Zhang, G. Wang, Z. Cai, G. W. Baxter, S. F. Collins, *Opt. Mater. Express.* **2016**, *6*, 3482.

[39] A. Ćirić, S. Stojadinović, M. D. Dramićanin, *Sens. Actuator A Phys.* **2019**, *295*, 450.

[40] M. A. Hernández-Rodríguez, A. D. Lozano-Gorrín, I. R. Martín, U. R. Rodríguez-Mendoza, V. Lavín, *Sens. Actuators, B* **2018**, *255*, 970.

[41] M. E. Köse, B. F. Carroll, K. S. Schanze, *Langmuir* **2005**, *21*, 9121.

[42] C. F. Chapman, Y. Liu, G. J. Sonek, B. J. Tromberg, *Photochem. Photobiol.* **1995**, *62*, 416.

**ADVANCED
SCIENCE NEWS**

www.advancedsciencenews.com

**ADVANCED
FUNCTIONAL
MATERIALS**

www.afm-journal.de

[43] C. Baleizão, S. Nagl, S. M. Borisov, M. Schäferling, O. S. Wolfbeis, M. N. Berberan-Santos, *Chem. Eur. J.* **2007**, *13*, 3643.

[44] C. Gota, S. Uchiyama, T. Yoshihara, S. Tobita, T. Ohwada, *J. Phys. Chem. B* **2008**, *112*, 2829.

[45] K. Okabe, N. Inada, C. Gota, Y. Harada, T. Funatsu, S. Uchiyama, *Nat. Commun.* **2012**, *3*, 705.

[46] O. A. Savchuk, J. J. Carvajal, M. C. Pujol, E. W. Barrera, J. Massons, M. Aguilo, F. Diaz, *J. Phys. Chem. C.* **2015**, *119*, 18546.

[47] M. K. Mahata, T. Koppe, K. Kumar, H. Hofsäss, U. Vetter, *Sci. Rep.* **2016**, *6*, 36342.

[48] A. Siaï, P. Haro-González, K. Horchani-Naifer, M. Férid, *Sens. Actuators, B* **2016**, *234*, 541.

[49] L. Marciniak, K. Trejgis, *J. Mater. Chem. C.* **2018**, *6*, 7092.

[50] S. Gharouel, L. Labrador-Páez, P. Haro-González, K. Horchani-Naifer, M. Férid, *J. Lumin.* **2018**, *201*, 372.

[51] M. Back, J. Ueda, M. G. Brik, T. Lesniewski, M. Grinberg, S. Tanabe, *ACS Appl. Mater. Interfaces.* **2018**, *10*, 41512.